



Revisiting the physical mechanisms of East Asian summer monsoon precipitation changes during the mid-Holocene: a data–model comparison

Yong Sun^{1,2,3} · Haibin Wu^{4,5,6} · Gilles Ramstein³ · Bo Liu⁷ · Yan Zhao¹ · Laurent Li⁸ · Xiayu Yuan⁹ · Wenchao Zhang⁴ · Lijuan Li² · Liwei Zou² · Tianjun Zhou^{2,10}

Received: 9 November 2021 / Accepted: 21 May 2022 / Published online: 17 June 2022
© The Author(s) 2022

Abstract

The mid-Holocene (MH; 6 ka) is one of the benchmark periods for the Paleoclimate Modeling Intercomparison Project (PMIP) and provides a unique opportunity to study monsoon dynamics and orbital forcing (i.e., mostly precession) that differ significantly from the present day. We conducted a data–model comparison along with a dynamic analysis to investigate monsoonal (i.e., East Asian summer monsoon; EASM) precipitation changes over East Asia during the MH. We used the three phases of the PMIP simulations for the MH, and quantitatively compare model results with pollen-based climate records. The data–model comparison shows an overall increase in the summer monsoon precipitation, except a local decrease during the MH. Decomposition of the moisture budget into thermodynamic and dynamic components allows us to assess their relative role in controlling EASM precipitation during the MH, and to investigate the precipitation changes obtained from pollen records in terms of physical processes. We show that the dynamic effect, rather than the thermodynamic effect, is the dominant control in increased EASM precipitation during the MH in both the proxy records and models. The dynamic increase in precipitation results mainly from the enhancement of horizontal monsoonal moisture transport that is caused by intensified stationary eddy horizontal circulation over East Asia. In addition, a cloud-related cooling effect reduced the thermodynamic contribution to the increase in EASM precipitation during the MH.

Keywords Mid-Holocene · Monsoon precipitation · Data–model comparison · Water vapor budget · Thermodynamic effect · Dynamic effect · Cloud cooling effect

✉ Yong Sun
yongsun@itpcas.ac.cn

¹ State Key Laboratory of Tibetan Plateau Earth System, Resources and Environment (TPESRE), Institute of Tibetan Plateau Research, Chinese Academy of Sciences, Beijing 100101, China

² State Key Laboratory of Numerical Modeling for Atmospheric Sciences and Geophysical Fluid Dynamics, Institute of Atmospheric Physics, Chinese Academy of Sciences, Beijing 100029, China

³ Laboratoire des Sciences du Climat et de l'Environnement, LSCE/IPSL, CEA-CNRS-UVSQ, Université Paris-Saclay, Gif-sur-Yvette, France

⁴ Key Laboratory of Cenozoic Geology and Environment, Institute of Geology and Geophysics, Chinese Academy of Sciences, Beijing 100029, China

⁵ CAS Center for Excellence in Life and Paleoenvironment, Beijing 100044, China

⁶ University of Chinese Academy of Sciences, Beijing 100049, China

⁷ Department of Atmospheric Science, School of Environmental Studies, China University of Geoscience, Wuhan 430074, China

⁸ Laboratoire de Météorologie Dynamique, CNRS, Sorbonne Université, Ecole Normale Supérieure, Ecole Polytechnique, Paris, France

⁹ Editorial Office of Advances in Atmospheric Sciences, Institute of Atmospheric Physics, Chinese Academy of Sciences, Beijing 100029, China

¹⁰ CAS Center for Excellence in Tibetan Plateau Earth Sciences, Chinese Academy of Sciences (CAS), Beijing 100101, China

1 Introduction

The mid-Holocene (MH; *ca.* 6 ka) is part of the current interglacial period. This period was characterized by a large change in precession, which led to an enhanced seasonal cycle, whereas greenhouse gases (GHGs) were similar to pre-industrial (PI) levels and continental configurations were almost identical to present day. Therefore, the MH is an ideal period for studying the orbital-forcing of Earth's climate (Steig 1999; Shin et al. 2006).

Paleoclimatic reconstructions and simulations based on the Paleoclimate Modeling Intercomparison Project (PMIP) protocols are important approaches for investigating large-scale MH climate features and the mechanisms driving climate changes. In general, data–model comparisons have shown similar annual mean monsoonal precipitation changes during the MH compared with the PI period (COHMAP Members 1988; Braconnot et al. 2012; Zhao and Harrison 2012; Jiang et al. 2015; Jiang et al. 2019; Lin et al. 2019; D'Agostino et al. 2019, 2020). Solar radiation increases (decreases) in the boreal (austral) summer acted as the main driver of strengthening (weakening) of the Northern (Southern) Hemisphere monsoon in the MH (Joussaume et al. 1999; Zhao and Harrison 2012; Jiang et al. 2015; Brierley et al. 2020). In addition to the direct response to solar forcing, regional monsoonal precipitation changes are also influenced by feedback from vegetation expansion, dust reduction (Patricola and Cook 2007; Pausata et al. 2016; Hopcroft and Valdes 2019; Piao et al. 2020), ice sheets (Yin et al. 2009; Lyu et al. 2021), and oceanic processes (Liu et al. 2004; Zhao et al. 2005; Zhao and Harrison 2012). The “Green Sahara” involved the northward extension of vegetation in North Africa during the MH, which increased Northern Hemisphere on-land monsoonal precipitation (Sun et al. 2019) and shifted the East Asian summer monsoon (EASM) northward (Piao et al. 2020). The vegetated Sahara induced changes in the Walker and Hadley circulations, enhanced the western Pacific subtropical high (WPSH), and strengthened the EASM (Piao et al. 2020).

An increasing number of studies have used dynamic diagnostics to improve our understanding of regional rainfall processes during the MH. Using a moisture budget analysis, D'Agostino et al. (2019) examined the impact of thermodynamic and dynamic components on the Northern Hemisphere monsoon response to MH orbital forcing, and found that dynamic processes were the dominant contributor to increased monsoon precipitation in the MH. This increase in precipitation due to the dynamic effect can largely be explained by enhanced vertical motion due to local diabatic heating of the atmospheric column (D'Agostino et al. 2019). Although D'Agostino

et al. (2019) did not consider the EASM due to the hybrid nature of tropical and subtropical monsoons with impacts from mid and high-latitudes (Ding and Chan 2005), their findings were found to be valid for the EASM by Wang et al. (2020). However, it remains unclear why the thermodynamic contribution to monsoon precipitation changes during the MH was weak. In addition to the key role of vertical moisture advection (Wang et al. 2020), it remains to be determined whether a dynamic increase in MH precipitation can be achieved through enhancement of horizontal monsoon circulation. In addition, the simulated EASM precipitation changes during the MH have not been validated by proxy records. Therefore, the response of the EASM climate to orbital forcing during the MH is not fully understood.

In this study, we first conducted a quantitative data–model comparison of EASM precipitation changes during the MH. We then reconciled the data–model comparison by comparing the spatial patterns of decomposed physical processes that affect the moisture budget with those of recorded and simulated EASM precipitation changes.

2 Materials and methods

2.1 Pollen-based reconstruction

Fossil pollen is a direct indicator of the past vegetation and has been widely used to reconstruct precipitation changes in the EASM region. Many well-dated Holocene pollen records in China provide an ideal opportunity to investigate the spatial–temporal patterns of past changes in precipitation.

We compiled 159 pollen records in China that include the mid-Holocene period (6000 ± 500 ^{14}C yr BP). This dataset comprises 65 original records from the China Quaternary Pollen Database (CQPD 2000), 3 original records compiled during the present study, and 91 records compiled from figures presented in previous paper (Lin et al. 2019). Our database improves the spatial coverage of vegetation and climate records in China.

We used the inverse vegetation model (IVM; Guiot et al. 2000; Wu et al. 2007) to undertake quantitative reconstructions of past changes in precipitation. IVM combines the vegetation model BIOME4 and pollen-based biome reconstructions via the inversion technique described by Guiot et al. (2000). For each sample, the output of the BIOME4 produced by systematically varying the values of input variables (i.e., ΔT , ΔP , and atmospheric CO_2 concentration) is compared with the biome scores calculated from pollen data (CQPD 2000). The suite of variables that yields the most similar biome data to the results from the pollen data is assigned to the fossil sample. The IVM has advantages in extracting

seasonal climate signals and provides a means to assess the influence of atmospheric CO₂ concentration on plant growth, and thus can provide reliable reconstructions of paleoclimate (Guiot et al. 2000; Wu et al. 2007; Lin et al. 2019). Further details of the IVM method were presented by Guiot et al. (2000) and Wu et al. (2007). The mid-Holocene precipitation reconstructions used in this study are from Lin et al. (2019) and can be seen in the online Supplementary Material (Table S1).

2.2 Three phases of PMIP simulations for MH climate

MH simulations from the three phases of PMIP (PMIP2, PMIP3, and PMIP4) were used to provide a dynamic understanding of EASM precipitation variations at orbital timescales. The same orbital parameter configurations (eccentricity = 0.018682; obliquity = 24.105°; angular precession = 0.87°) were used in all three PMIP phases for the MH, but in the PI runs slight differences in the reference periods were chosen for the three PMIP phases (Berger 1978; Braconnot et al. 2007, 2012; Otto-Bliesner et al. 2017). Orbital forcing of the PI runs in PMIP2 and PMIP3 was set to 1950, and the orbital parameters in 1850 were applied to the PI run in PMIP4.

In addition, there are two differences in GHG concentrations for PMIP4 compared with PMIP2 and PMIP3: (1) the same trace gas concentrations (CO₂ = 280 ppm; N₂O = 270 ppb) were used for the MH and PI periods under the PMIP2 and PMIP3 protocols, except for a reduction in CH₄ (from 760 ppb in the PI period to 650 ppb in the MH); (2) PMIP4 used different GHG concentrations for the PI period (CO₂ = 284.3 ppm; CH₄ = 808.2 ppb; N₂O = 273.0 ppb) and MH (CO₂ = 264.4 ppm; CH₄ = 597 ppb; N₂O = 262.0 ppb) simulations. In addition, the solar constant used by PMIP4 (1360.7 W/m²) is lower than that used in PMIP2 and PMIP3 (1365 W/m²). More details of the PMIP models and experimental parameters used for the MH simulations are presented in Tables S2, S3, and S4. In brief, the climate change during the MH obtained from PMIP simulations is broadly consistent with theory and observations, including increased summer warming of the Northern Hemisphere and associated shifts in tropical rainfall. Biases in the magnitude and sign of regional responses are similar in PMIP2, PMIP3, and PMIP4, despite the improvement of the models in complexity and resolution (Braconnot et al. 2012; Brierley et al. 2020).

In this study, we generally present findings based on the multi-model ensembles (MMEs) mean of PMIP3 and PMIP4, except for Fig. 1, which shows results from the MMEs of all three PMIP phases, because all three phases of PMIP yield similar surface climate simulations for East

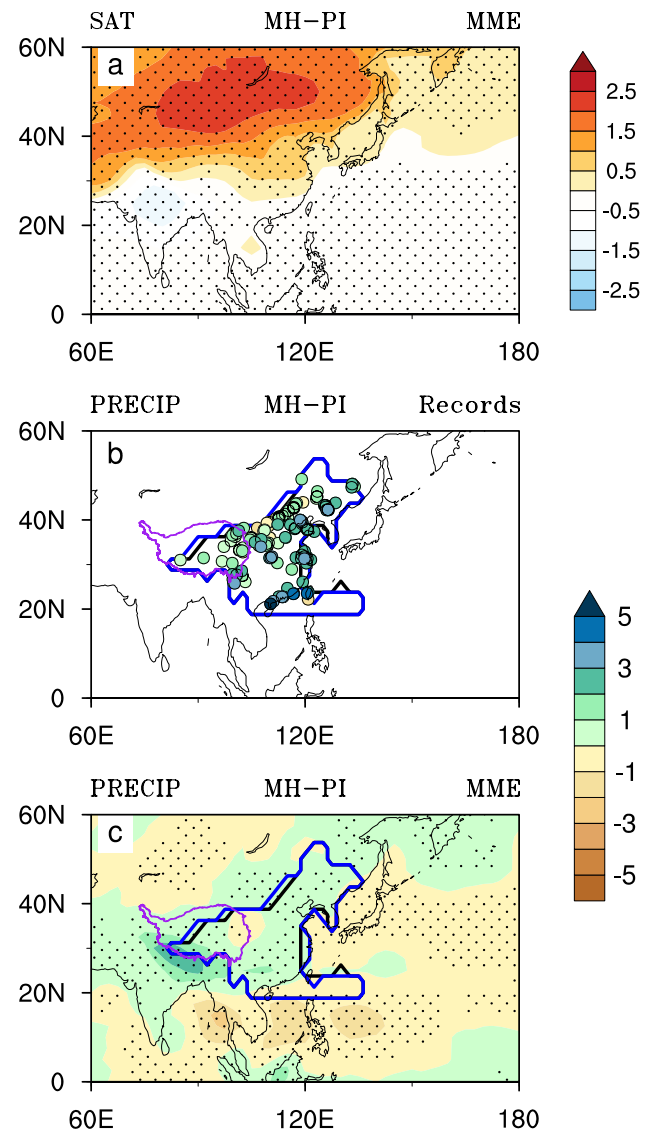


Fig. 1 Spatial patterns of mean June–July–August (JJA) surface air temperature (SAT in °C; top panel) and precipitation (PRECIP in mm/day) changes during the mid-Holocene (MH) compared with pre-industrial (PI) levels derived from pollen-based reconstructions (middle panel) and the multi-model ensemble (MME) of the three PMIP phases (bottom panel). Areas with a significance above the 1% level are stippled. Black and blue lines on the right panels are the East Asian Summer Monsoon (EASM) domain in the PI period and MH, respectively. The purple line outlines the Tibetan Plateau (data source: <http://www.geodoi.ac.cn/weben/doi.aspx?Id=135>). Colored circle symbols in (b) use the same color scale as the MME and represent pollen-based reconstructions (138 sites within the EASM domain) for the MH

Asia during the MH. The individual MME results for each PMIP phase are given in the online Supplementary Materials (Fig. S1).

2.3 Methodology

2.3.1 Moisture budget

The water vapor budget equation was used to constrain the physical processes that control the monsoonal precipitation variations on orbital timescales. The time-mean column-integrated moisture budget can be expressed as:

$$P = E - \langle \omega \partial_p q \rangle - \langle \vec{V} \cdot \nabla q \rangle + Res \quad (1)$$

where P is the precipitation, E is the evaporation, ω is the vertical velocity at a constant pressure coordinate, q is the atmospheric specific humidity, V is the horizontal wind velocity, and Res is a residual term including transient eddy effects and a contribution due to changes in surface moisture transport by the surface pressure gradient (Seager et al. 2010; Chou and Lan 2012; D'Agostino and Lionello 2020). Operator $\langle \cdot \rangle = \frac{1}{g\rho_w} \int_0^{P_s} \cdot dp$, where P_s is the surface pressure, ρ_w is the water density and g is the gravitational acceleration. In brief, the right side of Eq. 1 contains the local and remote moisture processes that contribute to monsoon precipitation (from left to right), which are evaporation, vertical moisture advection, horizontal moisture advection, turbulent moisture flux due to transient eddies, and surface moisture transport by the surface pressure gradient.

The difference in each term in Eq. 1 between the MH and PI periods can be written as follows:

$$\delta P = \delta E - \delta \langle \omega \partial_p q \rangle - \delta \langle \vec{V} \cdot \nabla q \rangle + \delta Res \quad (2)$$

To assess the relative importance of moisture content and atmospheric circulation changes on moisture transport, variations in the two advection terms were further decomposed into linear contributions from the thermodynamic component (TH) and dynamic component (DY). TH was calculated as an advective variation caused by changes in specific humidity with a fixed atmospheric circulation, and DY is represented by changes in atmospheric circulation at a constant specific humidity. Conventionally, transient eddy effects and their potential role in controlling EASM precipitation have not been addressed due to the unavailability of high-frequency (i.e., daily and sub-daily) outputs from most PMIP models. D'Agostino and Lionello (2020) presented an alternative approach to estimating the contribution of variations in transient eddies (δTE) to precipitation changes (δP) using the monthly output of PMIP models. This involves a non-linear contribution from the quadratic term due to the small effect as compared with the other terms or current unknowns in the underlying physics (Seager et al. 2010; Wills et al. 2016; D'Agostino and Lionello 2020). Equation 2 can be expressed as follows.

$$\delta P = \delta E + \delta TH + \delta DY + \delta TE + \delta S \quad (3)$$

$$\begin{aligned} \delta TH &= -\langle \vec{V} \cdot \nabla \delta q \rangle - \langle \omega \partial_p \delta q \rangle \\ &= -\frac{1}{g\rho_w} \int_0^{P_s} \vec{V} \cdot \nabla \delta q dp - \frac{1}{g\rho_w} \int_0^{P_s} \omega \partial_p \delta q dp \end{aligned} \quad (4)$$

$$\begin{aligned} \delta DY &= -\langle \delta \vec{V} \cdot \nabla q \rangle - \langle \delta \omega \partial_p q \rangle \\ &= -\frac{1}{g\rho_w} \int_0^{P_s} \delta \vec{V} \cdot \nabla q dp - \frac{1}{g\rho_w} \int_0^{P_s} \delta \omega \partial_p q dp \end{aligned} \quad (5)$$

$$\delta TE = \delta(P - E) - \delta TH - \delta DY - \delta S \quad (6)$$

$$\delta S = -\delta \nabla \cdot \langle q \vec{V} \rangle - \delta TH - \delta DY \quad (7)$$

2.3.2 Climate feedback response analysis method

The climate feedback response analysis method (CFRAM) was used to quantify the relative contributions of nine separate processes on surface temperature differences between the MH and PI periods. The CFRAM formula is (Cai and Lu 2009; Lu and Cai 2009):

$$\begin{aligned} \Delta \mathbf{T}_{MH-PI} &= \left(\frac{\partial \mathbf{R}}{\partial \mathbf{T}} \right)^{-1} (\Delta \mathbf{S}^{SI} + \Delta \mathbf{S}^{\alpha} + \Delta (\mathbf{S} - \mathbf{R})^{wv} \\ &\quad + \Delta (\mathbf{S} - \mathbf{R})^{cld} + \Delta (\mathbf{S} - \mathbf{R})^{CH_4} \\ &\quad + \Delta \mathbf{Q}^{SH} + \Delta \mathbf{Q}^{LH} + \Delta \mathbf{Q}^{AHT} + \Delta \mathbf{Q}^{Surface_dynamics}) \end{aligned} \quad (8)$$

where $\left(\frac{\partial \mathbf{R}}{\partial \mathbf{T}} \right)$ is the Planck feedback matrix and the superscripts SI, α , wv, cld, and CH_4 denote the surface temperature changes induced by solar insolation, surface albedo, water vapor, cloud, and methane, respectively. The superscripts SH, LH, AHT are the surface temperature changes due to surface sensible heat, latent heat fluxes, atmospheric heat transport. Surface dynamics represent the effect of land/ocean heat transport and are calculated as the residual term (Lu and Cai 2009; Liu et al. 2015). The advantage of this method is that it allows the actual processes that are responsible for the reduced thermodynamic increase in monsoonal precipitation to be distinguished (Figs. 2c, 3c, and 7e).

2.3.3 EASM domains

The EASM domains of this study follow the definition of Wang et al. (2012). The two required conditions are: (1) the annual range of precipitation rates (defined as local summer

Fig. 2 PMIP3-based results from the moisture budget equation used to resolve water vapor processes related to mean precipitation for the **a** MH and PI periods and **b** differences between the MH and PI periods. The two difference terms $(-\delta(\vec{V} \cdot \nabla q))$ and $-\delta(\omega \partial_p q)$ in **(b)** were decomposed into two processes in **(c)** to quantify the relative contribution from changes due to specific humidity with fixed atmospheric circulation (thermodynamic component; δTH [red bars]), and atmospheric circulation with constant specific humidity (dynamic component; δDY [blue bars]). In addition to quantifying the relative contributions of δTH and δDY , variations in transient eddies (δTE , [pink bars]) and surface quantities (δS , [gray bars]) in **(c)** that contribute to precipitation changes (δP) were estimated

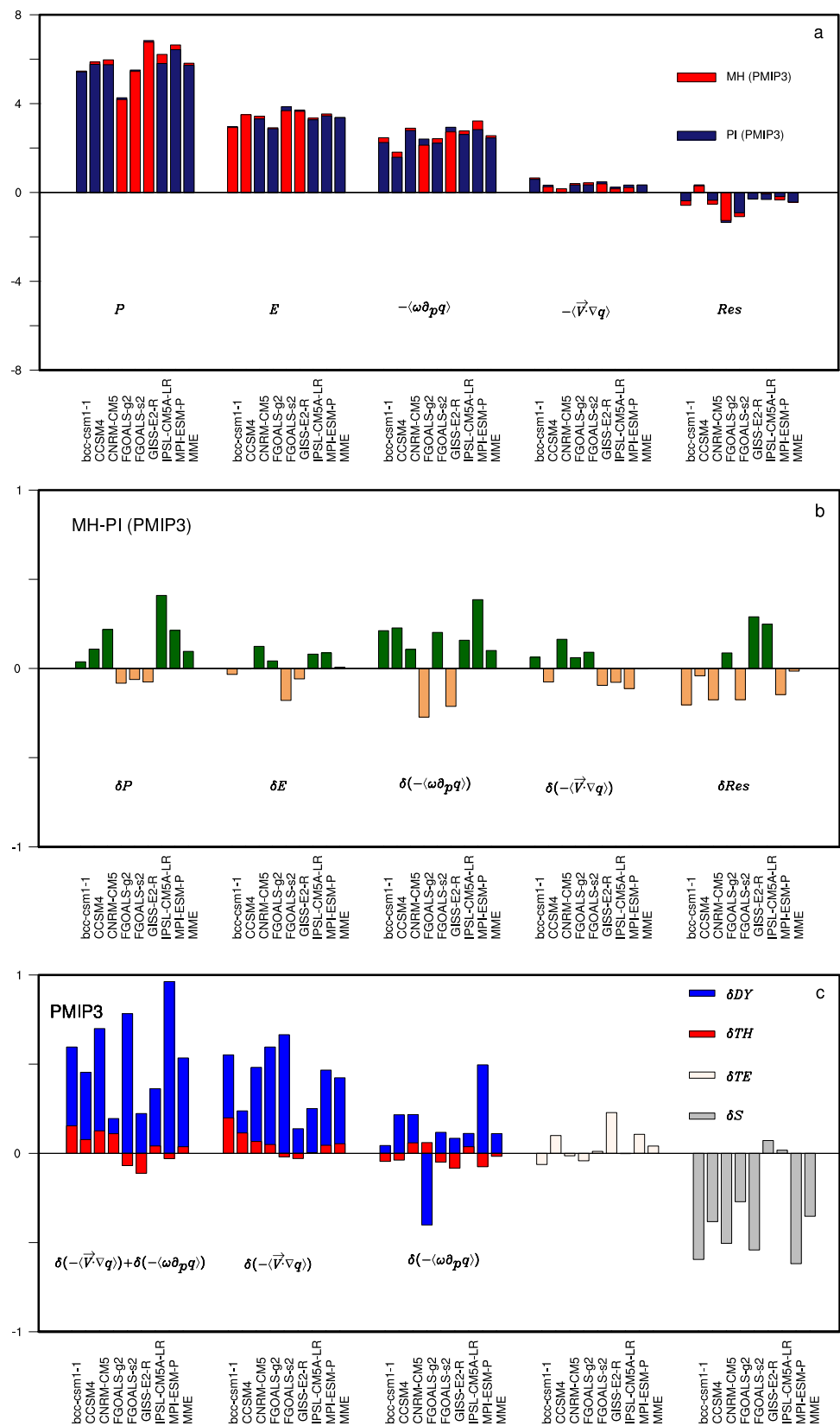
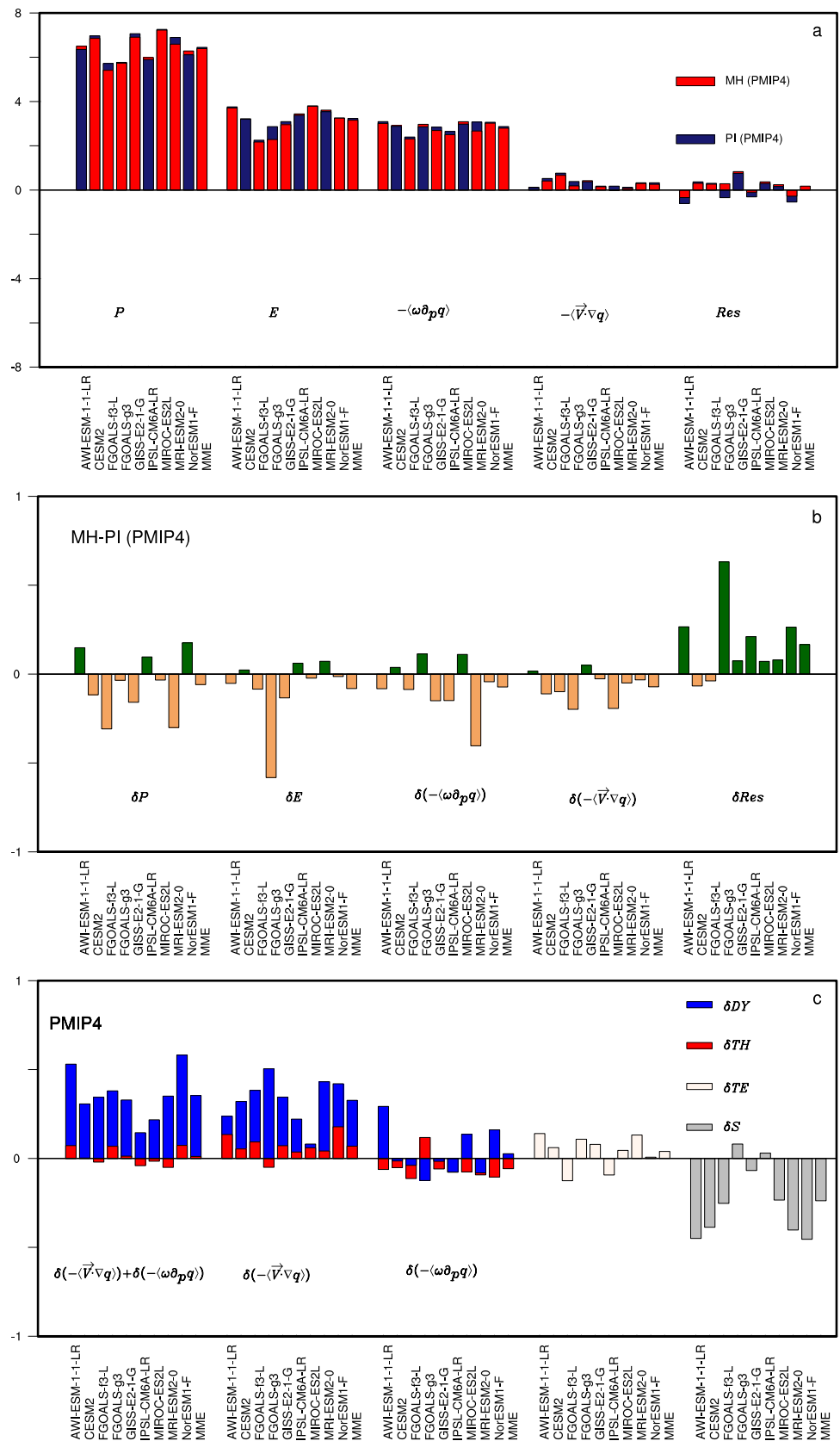


Fig. 3 As in Fig. 2, except that the moisture budget analyses are PMIP4 results



minus local winter) is > 2 mm/day; (2) the local summer precipitation is $> 55\%$ of total annual rainfall. The local summer includes May–June–July–August–September and local winter includes November–December–January–February–March. Given the inter-model spread of EASM domains across the MH and PI simulations, and slight differences in the EASM domains between the MH and PI periods, the results were averaged over the EASM domain of each model.

3 Results

3.1 Quantitative data–model comparison over the EASM domain

Figure 1 shows the surface air temperature (SAT) and precipitation (PRECIP) changes during the MH compared with the PI period. SAT changes during the MH are non-uniform across the EASM domain (Fig. 1a). This is reflected by southern cooling (south of 30°N) and northern warming (north of 30°N ; Fig. 1a). Consequently, these variations in SAT changes are associated with a reduction in meridional thermal contrast over the monsoonal domain, and its potential effects on the MH monsoonal precipitation are addressed in Sect. 3.3.1.

There is an overall increase in EASM precipitation during the MH, except for a decrease in a few parts of the monsoon area in both the proxy data and simulations (Figs. 1b, c and S1). Out of 138 pollen-based reconstruction sites, 119 show an EASM precipitation increase under the warm MH conditions (Fig. 1b), and the remaining 19 sites show a precipitation decrease (Fig. 1b). The quantitative records are consistent with the previous qualitative reconstruction (Lin et al. 2019). The PMIP models generate wetter (drier) MH than PI conditions over most (few) parts of the EASM domain (Figs. 1c and S1). However, there are distinct regions where the precipitation decreases during the MH (Figs. 1b, c and S1). Precipitation decrease in proxy data is mostly in northern China. Decreases in the modeled precipitation are confined to regions of the eastern Tibetan Plateau. In addition, there is large inter-model spread in an area-averaged EASM precipitation changes during the MH (Fig. S2).

We now use dynamic diagnostics to further examine the underlying cause of the spatial heterogeneity in simulated precipitation, and thus reconcile the data–model comparison.

3.2 Reconciling the data–model comparison by decomposition of the water vapor budget

3.2.1 Decomposing the physical processes involved in the simulated precipitation changes

An area-averaged moisture budget analysis was first undertaken over the EASM domain for the PI and MH periods (Figs. 2a, 3a, and S3a). Evaporation and vertical moisture advection were identified as being the dominant contributors to the mean summer precipitation over East Asia in the PI and MH periods, whereas the horizontal moisture advection and residual terms were less important. There are large inter-model variations for each moisture budget term (Figs. 2b, 3b, and S3b). To reveal the potential mechanisms for this range, and quantify the relative roles of horizontal and vertical moisture transports in controlling precipitation changes, further decomposition of the two moisture advection terms and an approximate breakdown of the residual term were carried out. Based on Eq. 3, the different influences of variations in evaporation (δE), thermodynamic contribution (δTH), dynamic contribution (δDY), transient eddies (δTE), and surface quantities (δS) lead to inter-model variability in EASM precipitation changes during the MH (Figs. 2b, c, 3b, c, and S3b). Despite the inter-model variations in each advection term, the signs are largely consistent among models (Figs. 2c, 3c, and S3b). For example, the two decomposed terms for total moisture advection (i.e., the sum of horizontal and vertical moisture advection) have a positive δDY value and negligible δTH value as compared with δDY . Therefore, the contrasting effects of δDY and δTH , in conjunction with the non-linear effect of the quadratic term involved in δTE (not shown) result in inter-model variability in the sign of each advection term. In addition, inter-model variations in residuals (δRes) can be largely explained by a net effect of negative δS value and negligible δTE values. A positive δDY value increases precipitation and a negative δS value leads to a precipitation decrease. There are distinct values for each decomposed process for the horizontal and vertical moisture advection (Figs. 2c and 3c). δDY (δS) has an overwhelming effect on the precipitation increase (decrease). This dynamic increase is due mainly to strengthening of the horizontal moisture advection. However, a much weaker precipitation increase is caused by the δTH of the horizontal moisture advection. In summary, the horizontal moisture advection has a dominant role in the total moisture advection.

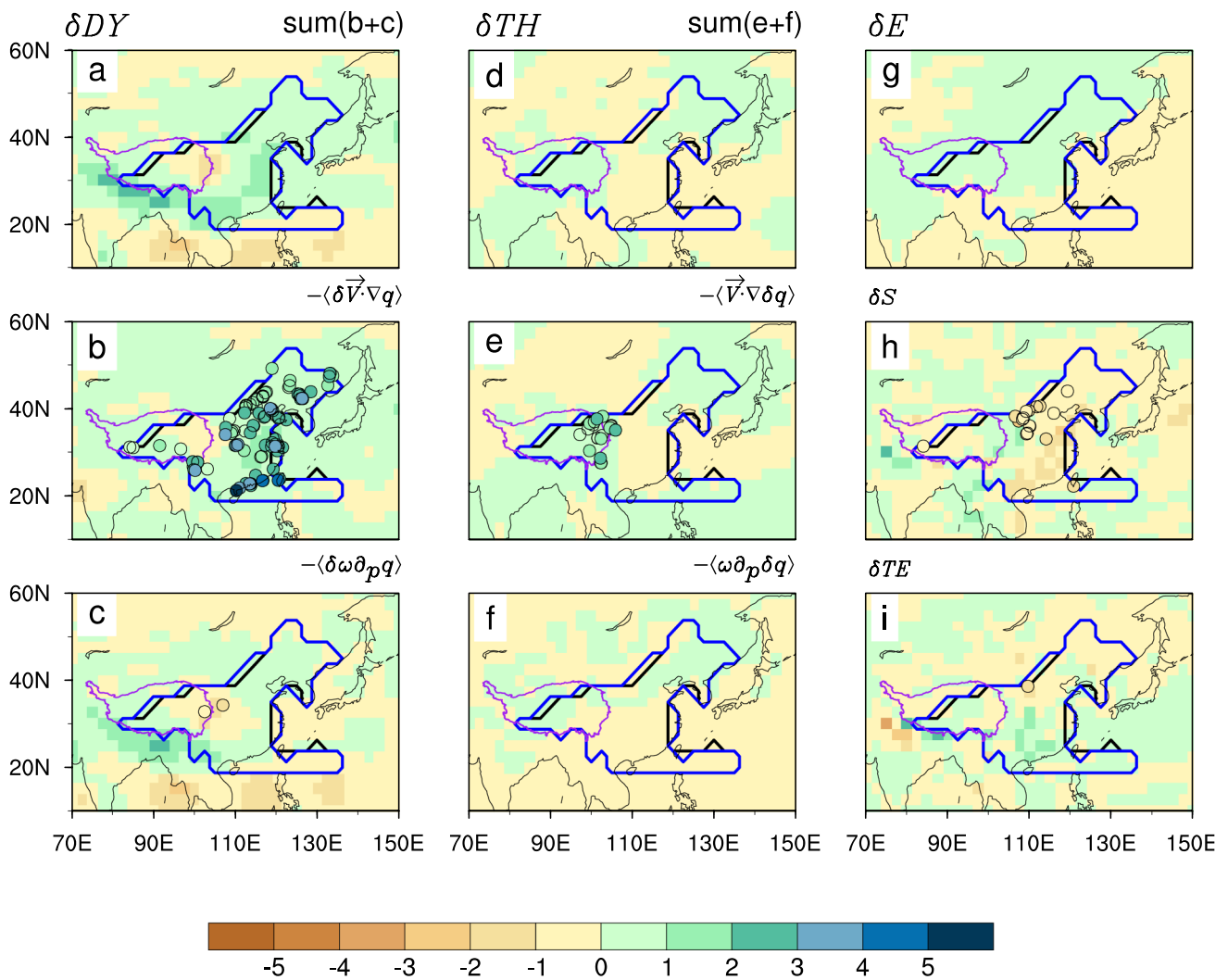


Fig. 4 Pollen-based precipitation records and spatial patterns of the five decomposed physical processes in Eq. 3 that contribute to precipitation changes (δP). **a, d, g, h, i** The physical processes (from left to right and top to bottom in each subfigure) are δDY , δTH , δE , δS , and δTE . **b, e** Horizontal moisture advection. **c, f** Vertical moisture

advection. **a, d** Sum of the two moisture advections. The 119 green circle symbols (99 in **(b)** and 20 in **(e)**) indicate wetter East Asia conditions, and the 19 yellow circle symbols (16 in **(h)**, 2 in **(c)** and 1 in **(i)**) indicate drier East Asia conditions

3.2.2 Decoding the physical representation of pollen-based precipitation records

Decomposition of the two moisture-advection types was used to understand the physical processes involved in pollen-based precipitation records. Figure 4 shows a quantitative comparison of the pollen-based precipitation record with the five decomposed processes in Eq. 3 (Fig. 4). The increase in precipitation from the proxy records are due mainly to intensified horizontal moisture advection (Fig. 4b). For example, 99 of 119 proxy records show a precipitation increase that can be explained by dynamic enhancement of horizontal moisture advection (Fig. 4b). The remaining 20 proxy records show a precipitation

increase that can be attributed to a weak increase in the TH of horizontal moisture advection (Fig. 4e). This is in good agreement with the limited role of TH in increasing precipitation (Figs. 2c and 3c). In contrast, a decrease in precipitation in 16 proxy records can be explained by the weakened surface quantities (Fig. 4h), and the remaining 3 records with drier MH conditions are generally consistent with a dynamic decrease in vertical moisture transport (Fig. 4c) and a weakening of transient eddies (Fig. 4i). In general, these results further support our previous modeling results, in that horizontal moisture advection is the dominant control on the increase in EASM precipitation during the MH.

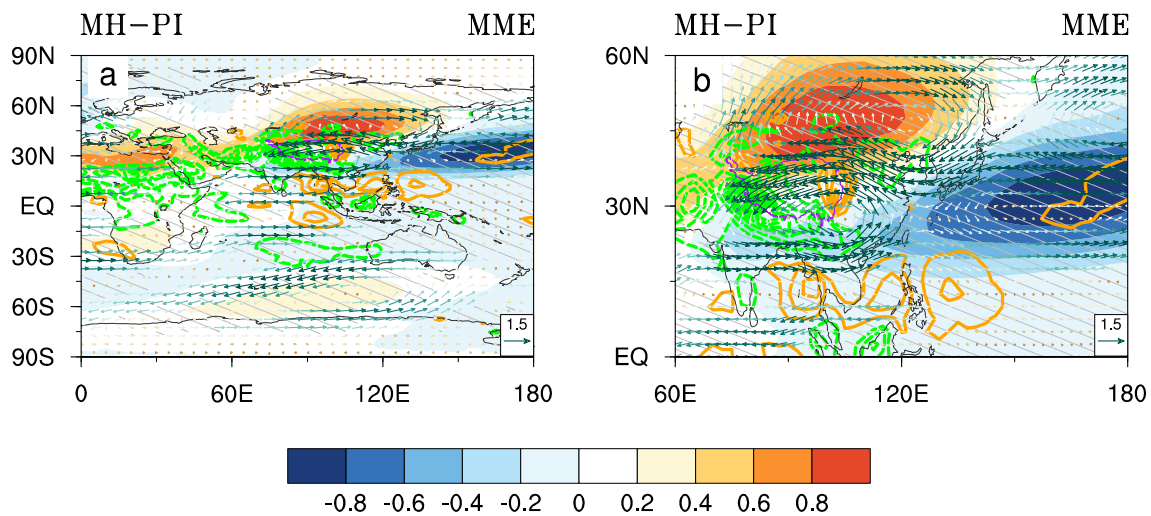


Fig. 5 **a** Differences between the three vertically integrated variables throughout the troposphere between the MH and PI periods, which are termed the stationary eddy horizontal circulation (colored vectors; color bar not shown), stationary eddy vertical velocity (contours), and air temperature (shading with color bar). **b** Enlarged view of (a) over

the EASM domain. Gray dashed lines are the stationary eddy air temperature above the 1% level. Positive vertical velocity values indicate descending motion (orange solid contours), and negative values represent ascending motion (green dashed contours)

3.3 Physics of the moisture budget decomposition

The moisture budget decomposition provides new insights into the data–model comparison. However, it is unclear what causes the dynamic enhancement of horizontal moisture advection and why the thermodynamic contribution to the precipitation increase is reduced during the MH. In addition, it is unknown whether the water vapor source of this dynamic enhancement has the same pathway as the EASM precipitation. Therefore, the physics underlying the thermodynamic and dynamic processes of horizontal moisture advection are further addressed in this section.

3.3.1 Mechanisms of dynamic control on the precipitation

The EASM domain and surrounding regions are dominated by stationary eddy horizontal circulation anomalies, as manifested by an anomalous cyclone confined to south of 30° N and a strong anticyclone to the north (Figs. S4 and 5a, b). The regional horizontal moisture advection is enhanced by the cyclonic control over the EASM domain, and thus leads to a dynamic increase in EASM precipitation during the MH (Fig. 5b). Prominent easterly anomalies are observed between the cyclone and anticyclone (30°–45° N). This westerly weakening (i.e., easterly anomalies) can be explained by the thermal wind balance and the reduced meridional thermal contrast (Fig. 1a). In fact, the stationary eddy cyclone and anticyclone that contribute to regional enhancement of horizontal moisture advection over the EASM domain are a key part of the global-scale stationary wave trains, which emanate from anticyclones at Northern

Hemisphere mid-latitudes to anticyclones at Southern Hemisphere mid-latitudes (Fig. 5a).

In contrast to the dynamic enhancement of horizontal moisture advection, the dynamic decrease of vertical moisture advection resulted in a drier eastern Tibetan Plateau during the MH (Figs. 1c, S1, and 4c). This DY decreased the precipitation over the eastern Tibetan Plateau due to the stationary eddy vertical motion in this region. Ascending motion characterizes the western Tibetan Plateau and a descending motion occurs in the eastern Tibetan Plateau (Fig. 5b). In addition to a decrease in local precipitation, stationary eddy-related regional meridional circulation characterizes the ascending motion along the Himalaya and the descending motion coincides with the ascending branch of the Hadley cell (i.e., ITCZ position; Fig. 5b). As a result, this anomalous regional meridional circulation resulted in a decrease in regional precipitation in the tropics (0°–20° N, 60°–150° E; Figs. 1c and S1).

3.3.2 Water vapor source sustaining the dynamic enhancement of the precipitation

Regional precipitation requires water vapor transport from source areas. In mean JJA conditions, cross-equatorial airflows originating in the southern Indian Ocean provide main source of water vapor for EASM precipitation during both PI and MH periods (Figs. 6a, b and S5; vectors and shading in the blue rectangular boxes). There is, however, an overall northward displacement of the strongest moisture transport belt during the MH as compared with PI (Fig. S6). This northward shift consequently leads to a marked dipole

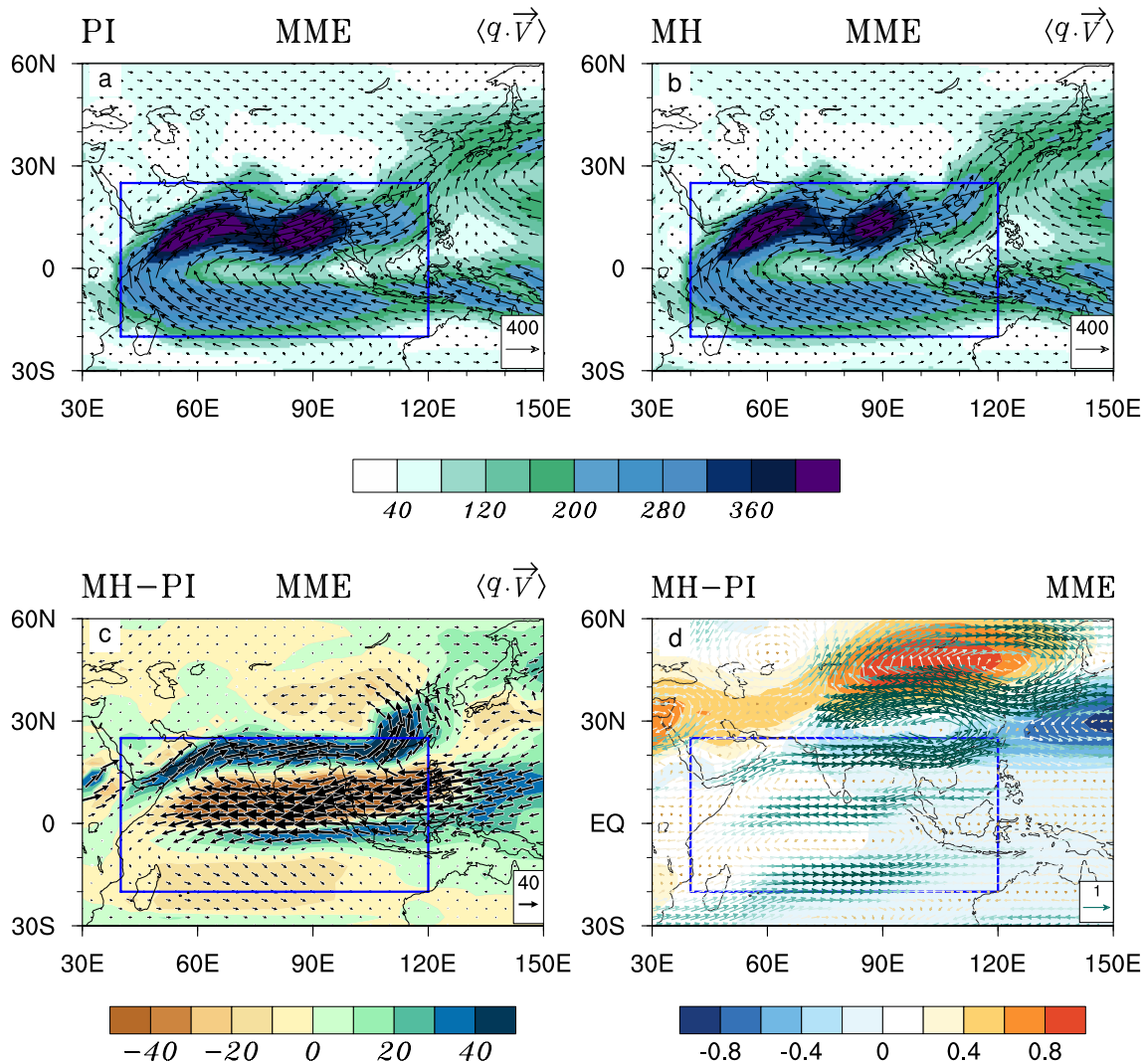


Fig. 6 Large-scale moisture transport as determined by the vertically integrated moisture flux ($\langle q \cdot \vec{V} \rangle$ in $\text{kg} \cdot \text{m}^{-1} \cdot \text{s}^{-1}$) across the whole troposphere in the boreal summer (JJA). Climatology of the **a** PI period and **b** MH period. **c** Differences between the MH and PI peri-

ods. **d** As for Fig. 5a, except that it shows an enlarged view of stationary eddy horizontal circulation and stationary eddy air temperature over the strongest moisture transport pathway responsible for EASM precipitation (blue rectangles in each plot)

structure for the moisture transport in each hemisphere (Fig. 6c; shading in the blue rectangular boxes) and forms a layered structure of moisture flux anomalies along the strongest water vapor pathway and adjacent oceanic areas (Fig. 6c; vectors in the blue rectangular boxes). Strengthening of the moisture transport occurs in the northernmost part of the layered structure and originates in south Asia and extends into the EASM domain. This water vapor pathway sustained the dynamic enhancement of EASM precipitation during the MH (Fig. 6c). Therefore, the tropical Indian Ocean in the Northern Hemisphere remains the main source of water vapor supply for the dynamic enhancement of the horizontal moisture transport during the MH. In contrast, there is a large reduction in the cross-equatorial airflow from

the southern Indian Ocean (on the southernmost margin of the layered structure), which is considered as the main water vapor supply source for the mean state of EASM precipitation (Fig. 6c). The middle part of the layered structure (5°S – 15°N) results from the combined effects of the northward moisture transport due to southwesterly airflow in the tropical northern Indian Ocean (the main effect) and the northward shift of the southeasterly airflow moisture transport in the tropical southern Indian Ocean. In summary, the overall northward shift of the moisture transport belt is mainly regulated by the stationary eddy wave train that determines the strongest water vapor pathways for EASM precipitation (Fig. 6d).

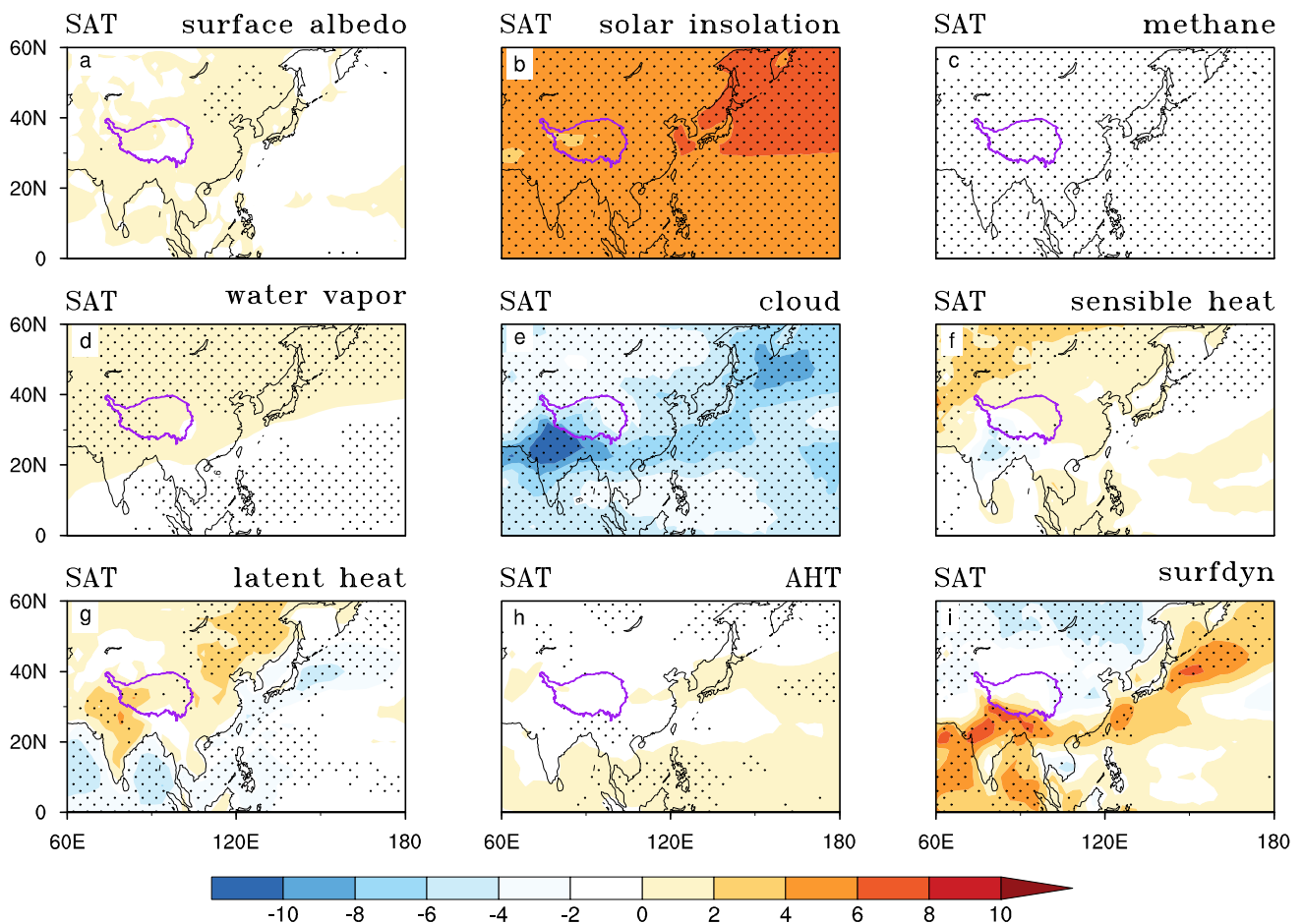


Fig. 7 CFRAM-based decompositions of SAT changes (in °C) in the MH relative to the PI period (as shown in Fig. 1a), as represented by nine processes. AHT and surfdyn in (h–i) are the atmospheric heat

transport and surface dynamic processes, respectively. This decomposition was derived from an MME of PMIP3. Stippled areas show that seven of the eight models have the same sign

3.3.3 Reduced thermodynamic role due to cloud cooling

The thermodynamic effect on precipitation is closely related to surface temperature changes. Therefore, quantifying the relative contribution of different processes to surface temperature changes with CFRAM (Cai and Lu 2009; Lu and Cai 2009) enables us to assess which processes affected surface temperature and, in turn, the reduced thermodynamic effect on precipitation. It would be expected that a thermodynamic increase (decrease) in precipitation is associated with surface warming (cooling). As such, the potential physical processes that cool Earth's surface are an underlying cause of the reduced thermodynamic role in the precipitation increase during the MH.

By decomposition of the “southern cooling and northern warming” pattern into nine processes (i.e., Fig. 1a versus Fig. 7), it was shown that the cloud-induced cooling (Fig. 7e) counteracts the main warming effect due to solar insolation (Fig. 7b), and thus leads to this “southern cooling and northern warming” pattern over China

(Fig. 7). The remaining five terms generally show either weak surface warming over mainland China (Fig. 7a, d, f, and g) in the absence of surface cooling required to sustain spatial heterogeneity (Fig. 1a), or an opposite pattern due to surface dynamic processes affecting the total SAT changes (Fig. 7i). In addition, surface cooling due to ATH and CH_4 is so weak that their contribution to the overall SAT changes can be ignored (Fig. 7c and h). In summary, in addition to their dominant role in the pattern of southern cooling and northern warming over East Asia, cloud-related processes were also dominant in controlling the global surface cooling (not shown). One remaining question is how the surface cooling due to cloudiness affected the monsoon precipitation.

Based on the Clausius–Clapeyron relationship, the atmospheric water vapor content decreases with cooling and increases with warming. The damping effect of cloud via the regional surface cooling causes water vapor decline in the atmosphere, and thus decreases the water supply available for precipitation. This is the primary reason for the weak

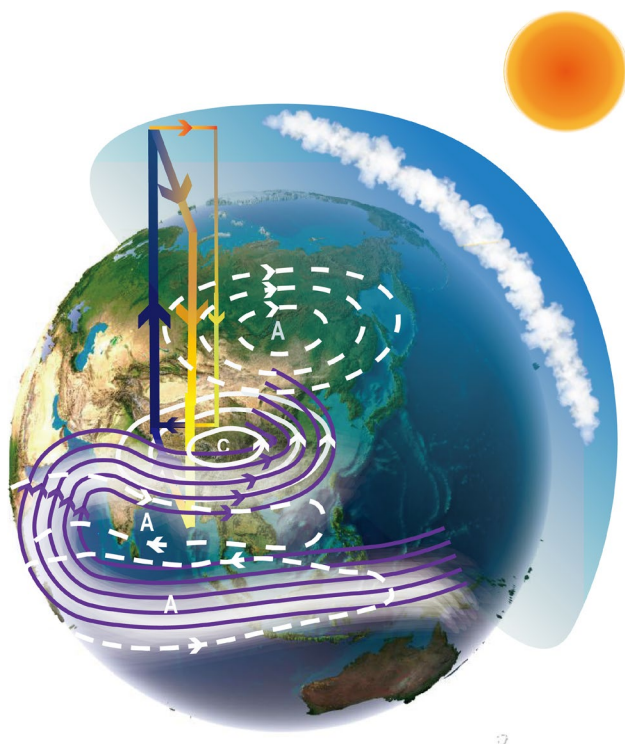


Fig. 8 Schematic illustration of the physics underlying monsoon precipitation responses to orbital forcing under MH climate conditions, including the dynamic strengthening and thermodynamic damping roles in an overall increase in EASM precipitation and a dynamic decrease in precipitation during the MH. Regional dynamic enhancement is part of the global-scale stationary eddy wave trains that consist of stationary eddy cyclones (C) and anticyclones (A) in the Northern and Southern Hemispheres. In addition to a regional dynamic enhancement, this wave train that forms in response to orbital forcings (mostly precession) results in an overall northward shift of the strongest water–vapor supply during the MH (purple lines with arrows) compared with the PI period (water vapor belt indicated by white shading). The thermodynamic contribution to the increase in precipitation is reduced by the cloud cooling effect. The figure also shows stationary-eddy related zonal and meridional circulations that result in reduced local and regional precipitation

thermodynamic effect during the MH. This cloud-related effect, particular in MH, contrasts with the significant thermodynamic effect on EASM precipitation increase/decrease in other warm/cold climates (Sun et al. 2016, 2018, 2021).

4 Summary and conclusions

We used proxy data and PMIP simulations to analyze orbital-scale climate variations in the EASM during the MH, when precession was quite different from the present day. Our results revealed distinct monsoonal dynamics at the orbital scale from those projected for future climate (Sun et al. 2018). Horizontal moisture advection controlled EASM precipitation changes during the MH in both the

proxy records and models. Our findings thus help reconcile proxy records and models for the regional precipitation changes in East Asia during the MH. Figure 8 summarizes our key findings which are:

1. A quantitative data–model comparison revealed heterogeneity in the MH surface climate over the EASM domain. There was an overall increase in precipitation in both proxy data and models, except for a few areas where there was a local decrease, which was associated with a reduction in meridional thermal contrast (i.e., the southern cooling and northern warming pattern) over the EASM domain.
2. By decomposing the moisture budget, we developed a physical understanding of the spatial heterogeneity of EASM precipitation changes in proxy data and models. Compared with the vertical moisture advection, the horizontal moisture advection played a larger role in determining the overall regional increase and local decrease in precipitation. The dynamic enhancement of horizontal moisture advection can explain the overall increase in precipitation in the simulations and most of the wetter MH proxy records (99 of 119) over the EASM domain. The remaining proxy records of wetter East Asia conditions resulted from a weak thermodynamic contribution to increasing horizontal moisture advection. In contrast, localized decreases in precipitation from the proxy records and models are controlled by different processes. Drier MH conditions (16 of 19 records) in proxy data mainly reflect a decrease in the surface quantities; the few records with precipitation decrease can be explained by a dynamic decrease in the vertical moisture transport (2 of 19 records) and weakened transient eddies (1 of 19 records), while dynamic decrease in vertical moisture advection generated a drier eastern Tibetan Plateau in simulations.
3. Stationary eddy activity is a mechanism that dynamically controls the regional precipitation. The dynamic enhancement of horizontal moisture advection that increased EASM precipitation was due mainly to the intensification of stationary eddy horizontal circulation over the EASM domain during the MH. In contrast, a dynamic decrease in the stationary eddy vertical motion resulted in a drier eastern Tibetan Plateau in the MH.
4. The cloud cooling effect was the dominant process responsible for the surface temperature decrease over the EASM domain, and is thus dominant in producing a southern cooling and northern warming pattern over China. Surface cooling due to cloud processes might have caused a reduction in the thermodynamic contribution to horizontal moisture advection and an increase in precipitation during the MH.

5. The tropical Indian Ocean in the Northern Hemisphere was the water vapor supply source for the dynamic enhancement of horizontal moisture transport, whereas water vapor transport from the strongest pathway (i.e., the cross-equatorial airflow from the southern Indian Ocean) maintaining the mean state of EASM was reduced during the MH. The layered structure of moisture transport anomalies due to the northward shift of the strongest moisture transport belt was regulated by the orbital forcing (i.e., mostly precession) during the MH. This modified the stationary eddy wave train along the strongest water vapor pathway responsible for the EASM precipitation.
6. As one reviewer concern, we also examined the impact of variation in land surface vegetation (Fig. A1) on shaping the thermodynamic and dynamic roles in precipitation during the MH (Figs. A2–A5). Compared with MH simulation using pre-industrial vegetation following PMIP4 protocol, the sensitivity simulation prescribed with reconstructed MH vegetation increases precipitation over most part of China except that decreases in Southeast Coast of China (Fig. A2). The spatial heterogeneity of EASM precipitation changes in response to vegetation change during the MH are mainly regulated by two distinct dynamic processes (Figs. A3–A5). i.e., dynamic enhancement of horizontal moisture advection generally strengthens the precipitation over China (Fig. A5), whereas dynamic decrease in precipitation over China Southeast Coasts is achieved through weakening of vertical motion (Fig. A5).

Supplementary Information The online version contains supplementary material available at <https://doi.org/10.1007/s00382-022-06359-1>.

Acknowledgements We thank the World Climate Research Program's Working Group on Coupled Modeling, which is responsible for CMIP, and the climate modeling groups for producing and making available their model outputs. All the simulations are publicly available on a website (https://www.ipcc-data.org/sim/gcm_monthly/AR5/Reference-Archive.html and <https://esgf-node.llnl.gov/projects/cmip6/>). Pollen-based reconstructions are open access (Table S1). We also thank Camille Risi from the Laboratoire de Météorologie Dynamique, Paris and Xu Zhang from Institute of Tibetan Plateau Research, Chinese Academy of Sciences for insightful comments on an earlier version of our manuscript. This research was jointly supported by the National Key Research and Development Program of China (Grant 2018YFA0606003), National Program on Key Basic Research Project of China (Grant 2017YFA0604601), Second Tibetan Plateau Scientific Expedition and Research (STEP) program (Grant 2019QZKK0102), and NSFC (Grants 41505076 and 41572165). Co-authors from French institutions acknowledge GENCI for allocation of computing resources.

Funding This work was funded by National Key Research and Development Program of China (Grant 2018YFA0606003), National Program on Key Basic Research Project of China (Grant 2017YFA0604601), Second Tibetan Plateau Scientific Expedition and Research (STEP) program (Grant 2019QZKK0102), and NSFC (Grants 41505076 and 41572165).

Data availability Both records and simulations involved in this study are open access to retrieve as described in acknowledgements.

Declaration

Conflict of interest The authors declare that they have no conflict of interests.

Open Access This article is licensed under a Creative Commons Attribution 4.0 International License, which permits use, sharing, adaptation, distribution and reproduction in any medium or format, as long as you give appropriate credit to the original author(s) and the source, provide a link to the Creative Commons licence, and indicate if changes were made. The images or other third party material in this article are included in the article's Creative Commons licence, unless indicated otherwise in a credit line to the material. If material is not included in the article's Creative Commons licence and your intended use is not permitted by statutory regulation or exceeds the permitted use, you will need to obtain permission directly from the copyright holder. To view a copy of this licence, visit <http://creativecommons.org/licenses/by/4.0/>.

References

- Berger A (1978) Long-term variations of daily insolation and quaternary climatic changes. *J Atmos Sci* 35:2362–2367
- Braconnot P, Otto-Bliessner B, Harrison S, Joussaume S, Peterchmitt J-Y, Abe-Ouchi A, Crucifix M, Driesschaert E, Fichetef T, Hewitt CD, Kageyama M, Kitoh A, Laine A, Loutre M-F, Marti O, Merkel U, Ramstein G, Valdes P, Weber SL, Yu Y, Zhao Y (2007) Results of PMIP2 coupled simulations of the mid-Holocene and Last Glacial Maximum—part 1: experiments and large-scale features. *Clim past* 3(2):261–277
- Braconnot P, Harrison SP, Kageyama M, Bartlein PJ, Masson-Delmotte V, Abe-Ouchi A, Otto-Bliessner B, Zhao Y (2012) Evaluation of climate models using palaeoclimatic data. *Nat Clim Change* 2:417–424
- Brierley C, Zhao A, Harrison S, Braconnot P, Williams C, Thornalley D, Shi X, Peterschmitt J-Y, Ohgaito R, Kaufman D, Kageyama M, Hargreaves J, Erb M, Emile-Geay J, Dagostino R, Chandan D, Carré M, Bartlein P, Zheng W, Zhang Z, Zhang Q, Yang H, Volodin E, Tomas R, Routson C, Peltier W, Otto-Bliessner B, Morozova P, McKay N, Lohmann G, Legrande A, Guo C, Cao J, Brady E, Annan J, Abe-Ouchi A (2020) Large-scale features and evaluation of the PMIP4-CMIP6 *midHolocene* simulations. *Clim past Discuss*. <https://doi.org/10.5194/cp-2019-168>
- Cai M, Lu JH (2009) A new framework for isolating individual feedback processes in coupled general circulation climate models. Part II: method demonstrations and comparisons. *Clim Dyn* 32:887–900
- Chou C, Lan CW (2012) Changes in the annual range of precipitation under global warming. *J Clim* 25(1):222–235. <https://doi.org/10.1175/JCLI-D-11-00097.1>
- D'Agostino R, Lionello P (2020) The atmospheric moisture budget in the Mediterranean: mechanisms for seasonal changes in the Last Glacial Maximum and future warming scenario. *Quat Sci Rev* 241:106392. <https://doi.org/10.1016/j.quascirev.2020.106392>
- D'Agostino R, Bader J, Bordoni S, Ferreira D, Jungclaus J (2019) Northern Hemisphere monsoon response to mid-Holocene orbital forcing and greenhouse gas-induced global warming. *Geophys Res Lett* 46:1591–1601
- D'Agostino R, Brown JR, Moise A, Nguyen H, Jungclaus J (2020) Contrasting Southern Hemisphere monsoon response:

- MidHolocene orbital forcing versus future greenhouse gas-induced global warming. *J Clim* 33(22):9595–9613
- Ding Y, Chan J (2005) The East Asian summer monsoon: an overview. *Meteorol Atmos Phys* 89:117–142
- Guiot J, Torre F, Jolly D, Peyron O, Boreux JJ, Cheddadi R (2000) Inverse vegetation modeling by Monte Carlo sampling to reconstruct palaeoclimates under changed precipitation seasonality and CO₂ conditions: application to glacial climate in Mediterranean region. *Ecol Model* 127:119–214
- Harrison S (2017) BIOME 6000 DB classified plotfile version 1. University of reading. Dataset. <https://doi.org/10.17864/1947.99>
- Hopcroft P, Valdes P (2019) On the role of dust-climate feedbacks during the mid-Holocene. *Geophys Res Lett* 46:1612–1621
- Jiang D, Tian Z, Lang X (2015) Mid-Holocene global monsoon area and precipitation from PMIP simulations. *Clim Dyn* 44:2493–2512
- Jiang W, Leroy SAG, Yang S, Zhang E, Wang L, Yang X, Rioual P (2019) Synchronous strengthening of the Indian and East Asian monsoons in response to global warming since the last deglaciation. *Geophys Res Lett* 46:3944–3952
- Joussaume S, Taylor K, Braconnot P, Mitchell J, Kutzbach J, Harrison S, Prentice I, Broccoli A, Abe-Ouchi A, Bartlein P, Bonfils C, Dong B, Guiot J, Herterich K, Hewitt C, Jolly D, Kim J, Kislov A, Kitoh A, Loutre M, Masson V, McAvaney B, McFarlane N, de Noblet N, Peltier W, Peterschmitt J-Y, Pollard D, Rind D, Royer J, Schlesinger M, Syktus J, Thompson S, Valdes P, Vettoretti G, Webb R, Wyputta U (1999) Monsoon changes for 6000 years ago: results of 18 simulations from the Palaeoclimate Modelling Intercomparison Project (PMIP). *Geophys Res Lett* 26:859–862
- Lin Y, Ramstein G, Wu H, Rani R, Braconnot P, Kageyama M, Li Q, Luo Y, Zhang R, Guo Z (2019) Mid-Holocene climate change over China: model–data discrepancy. *Clim past* 15(4):1223–1249
- Liu Z, Harrison S, Kutzbach J, Otto-Bliesner B (2004) Global monsoons in the mid-Holocene and oceanic feedback. *Clim Dyn* 22:157–182
- Liu B, Zhou T, Lu J (2015) Quantifying contributions of model processes to the surface temperature bias in FGOALS-g2. *J Adv Model Earth Syst* 7:1519–1533
- Lu J, Cai M (2009) A new framework for isolating individual feedback processes in coupled general circulation climate models. Part I: formulation. *Clim Dyn* 32:873–885
- Lyu AQ, Yin QZ, Crucifix M, Sun YB (2021) Diverse regional sensitivity of summer precipitation in East Asia to ice volume, CO₂ and astronomical forcing. *Geophys Res Lett* 48:e2020GL092005
- Members COHMAP (1988) Climatic changes of the last 18,000 years: observations and model simulations. *Science* 241:1043–1052
- Members of China Quaternary Pollen Data Base (MCQPD) (2000) Pollen-based Biome Reconstruction at Middle Holocene (6 ka BP) and Last Glacial Maximum (18 ka BP) in China. *J Integr Plant Biol* 42:1201–1209 (in Chinese with English abstract)
- Otto-Bliesner BL et al (2017) The PMIP4 contribution to CMIP6—Part 2: two interglacials, scientific objective and experimental design for Holocene and Last Interglacial simulations. *Geosci Model Dev* 10:3979–4003
- Patricola C, Cook K (2007) Dynamics of the West African Monsoon under mid-Holocene precessional forcing: regional climate model simulations. *J Clim* 20:694–716
- Pausata F, Messori G, Zhang Q (2016) Impacts of dust reduction on the northward expansion of the African monsoon during the Green Sahara period. *Earth Planet Sci Lett* 434:298–307
- Piao J, Chen W, Wang L, Pausata F, Zhang Q (2020) Northward extension of the East Asian summer monsoon during the mid-Holocene. *Glob Planet Change*. <https://doi.org/10.1016/j.gloplacha.2019.103046>
- Prentice IC, Webb T (1998) BIOME 6000: reconstructing global mid-Holocene vegetation patterns from palaeoecological records. *J Biogeogr* 25(6):997–1005
- Prentice C, Guiot J, Huntley B, Jolly D, Cheddadi R (1996) Reconstructing biomes from palaeoecological data: a general method and its application to European pollen data at 0 and 6 ka. *Clim Dynam* 12:185–194
- Seager R, Naik N, Vecchi GA (2010) Thermodynamic and dynamic mechanisms for large-scale changes in the hydrological cycle in response to global warming. *J Clim* 23(17):4651–4668
- Shin S-I, Sardeshmukh PD, Webb RS, Oglesby RJ, Barsugli JJ (2006) Understanding the mid-Holocene climate. *J Clim* 19:2801–2817. <https://doi.org/10.1175/JCLI3733.1>
- Steig E (1999) Mid-Holocene climate change. *Science* 286:148–149
- Sun Y, Zhou T, Ramstein G, Contoux C, Zhang Z (2016) Drivers and mechanisms for enhanced summer monsoon precipitation over East Asia during the mid-Pliocene in the IPSL-CM5A. *Clim Dyn* 46:1437–1457
- Sun Y, Ramstein G, Li L, Contoux C, Tan N, Zhou T (2018) Quantifying East Asian summer monsoon dynamics in the ECP4.5 scenario with reference to the mid-Piacenzian warm period. *Geophys Res Lett* 45:12523–12533
- Sun W, Wang B, Zhang Q, Pausata F, Chen D, Lu G, Yan M, Ning L, Liu J (2019) Northern Hemisphere land monsoon precipitation increased by the Green Sahara during middle Holocene. *Geophys Res Lett* 46:9870–9879
- Sun Y, Wu H, Kageyama M, Ramstein G, Li L, Tan N, Lin Y, Liu B, Zheng W, Zhang W, Zou L, Zhou T (2021) The contrasting effects of thermodynamic and dynamic processes on East Asian summer monsoon precipitation during the Last Glacial Maximum: a data-model comparison. *Clim Dyn* 56:1303–1316
- Wang B, Liu J, Kim H, Webster P, Yim S (2012) Recent change of the global monsoon precipitation (1979–2008). *Clim Dyn* 39:1123–1135
- Wang N, Jiang D, Lang X (2020) Mechanisms for spatially inhomogeneous changes in East Asian Summer Monsoon precipitation during the mid-Holocene. *J Clim* 33:2945–2965
- Wills RC, Byrne MP, Schneider T (2016) Thermodynamic and dynamic controls on changes in the zonally anomalous hydrological cycle. *Geophys Res Lett* 43:4640–4649
- Wu H, Guiot J, Brewer S, Guo Z (2007) Climatic changes in Eurasia and Africa at the last glacial maximum and mid-Holocene: reconstruction from pollen data using inverse vegetation modelling. *Clim Dyn* 29(2):211–229
- Yin QZ, Berger A, Crucifix M (2009) Individual and combined effects of ice sheets and precession on MIS-13 climate. *Clim past* 5:229–243
- Zhao Y, Harrison SP (2012) Mid-Holocene monsoons: a multi-model analysis of the inter-hemispheric differences in the response to the orbital forcing and ocean feedbacks. *Clim Dyn* 39:1457–1487
- Zhao Y, Braconnot P, Marti O, Harrison S, Hewitt C, Kitoh A, Liu Z, Mikolajewicz U, Otto-Bliesner B, Weber S (2005) A multimodel analysis of role of ocean feedback on the African and Indian monsoon during Mid-Holocene. *Clim Dyn* 25:777–800

Publisher's Note Springer Nature remains neutral with regard to jurisdictional claims in published maps and institutional affiliations.